Anodic Electrochemistry of Mono- and Dinuclear Aminophenylferrocene and Diphenylaminoferrocene Complexes

Ming-Xing Zhang,[†,§] Jing Zhang,[†,¶,§] Jun Yin,[†] František Hartl,[*,‡] Sheng-Hua Liu[*,†]

[†]*Key Laboratory of Pesticide and Chemical Biology, Ministry of Education, College of Chemistry, Central China Normal University, Wuhan 430079, P.R. China*

[¶] *College of Chemistry, The Hong Kong University of Science and Technology, Clear Water Bay, Kowloon, Hong Kong*

[‡]*Department of Chemistry, University of Reading, Whiteknights, Reading RG6 6AD, UK*

[§]These authors contributed equally to this work.

Table S1. Crystal data and parameters of data collection and refinement for complex **1d**.

Complex	**1d**
Formula	$C_{24}H_{23}FeNO_2$
Formula weight	413.28
Temperature (K)	296 (2)
Crystal system	Monoclinic
Space group	*P*2(1)/*c*
a (Å)	17.7696 (18)
b(Å)	9.6825 (10)
c(Å)	22.947 (2)
α (°)	90
β (°)	92.595 (2)
γ (°)	90
V (Å^3)	3944.1 (7)
Z	8
Density (calculated) (Mg/m^3)	1.392
Absorption coefficient (mm^{-1})	0.784
F(000)	1728
Crystal size (mm^3)	0.20 × 0.10 × 0.10
Theta range for data collection (°)	1.78 to 27.45
Index ranges	$-23\leq h\leq 23$, $-12\leq k\leq 12$, $-29\leq l\leq 29$
Reflections collected	32836
Independent reflections	8967 [*R*(int) = 0.0562]
Max. and min. transmission	0.9257 and 0.9118
Data / restraints / parameters	8967 / 0 / 510
Goodness-of-fit on F^2	0.997
Final *R* indices [$I>2\sigma(I)$]	*R*1 = 0.0443, *wR*2 = 0.1093
R indices (all data)	*R*1 = 0.0826, *wR*2 = 0.1266
Largest diff. peak and hole (e.$^{-3}$)	0.279 and -0.336

Table S2. Bond lengths [Å] and angles [deg] for complex **1d**.

Bond lengths [Å]			
Fe1—C3	2.028 (3)	C7—C8	1.410 (4)
Fe1—C2	2.034 (2)	C11—C16	1.369 (4)
Fe1—C10	2.036 (3)	C11—C12	1.383 (3)
Fe1—C4	2.038 (3)	O1—C14	1.372 (3)
Fe1—C9	2.038 (3)	O1—C17	1.408 (4)
Fe1—C7	2.040 (3)	C19—C20	1.369 (4)
Fe1—C6	2.040 (3)	C2—C3	1.416 (4)
Fe1—C8	2.044 (3)	C21—C22	1.382 (4)
Fe1—C5	2.061 (3)	C21—C20	1.386 (4)
Fe1—C1	2.072 (2)	C9—C8	1.403 (4)
N1—C1	1.411 (3)	C9—C10	1.408 (4)
N1—C18	1.425 (3)	C10—C6	1.415 (4)
N1—C11	1.439 (3)	C13—C12	1.376 (4)
O2—C21	1.373 (3)	C13—C14	1.378 (4)
O2—C24	1.421 (3)	C22—C23	1.383 (4)
C18—C23	1.387 (3)	C16—C15	1.387 (4)
C18—C19	1.394 (3)	C15—C14	1.379 (4)
C1—C2	1.422 (4)	C4—C3	1.405 (4)
C1—C5	1.425 (4)	C4—C5	1.421 (4)
C7—C6	1.403 (4)	C7—C8	1.410 (4)
Bond angles [deg]			
C3—Fe1—C2	40.79 (10)	C8—Fe1—C1	152.56 (11)
C3—Fe1—C10	153.66 (13)	C5—Fe1—C1	40.34 (10)
C2—Fe1—C10	164.75 (12)	C1—N1—C18	124.0 (2)
C3—Fe1—C4	40.45 (12)	C1—N1—C11	114.3 (2)
C2—Fe1—C4	68.27 (11)	C18—N1—C11	117.4 (2)
C10—Fe1—C4	120.30 (13)	C21—O2—C24	117.2 (2)
C3—Fe1—C9	119.25 (12)	C23—C18—C19	117.4 (2)
C2—Fe1—C9	152.74 (13)	C23—C18—N1	124.1 (2)

C10—Fe1—C9	40.45 (13)	C19—C18—N1	118.5 (2)
C4—Fe1—C9	109.02 (12)	N1—C1—C2	123.4 (2)
C3—Fe1—C7	126.54 (12)	N1—C1—C5	129.1 (2)
C2—Fe1—C7	107.12 (11)	C2—C1—C5	107.4 (2)
C10—Fe1—C7	67.95 (12)	N1—C1—Fe1	130.19 (17)
C4—Fe1—C7	164.45 (13)	C2—C1—Fe1	68.32 (14)
C9—Fe1—C7	67.84 (12)	C5—C1—Fe1	69.40 (15)
C3—Fe1—C6	163.97 (12)	C6—C7—C8	108.2 (3)
C2—Fe1—C6	126.45 (11)	C6—C7—Fe1	69.89 (16)
C10—Fe1—C6	40.64 (12)	C8—C7—Fe1	69.96 (17)
C4—Fe1—C6	154.30 (13)	C16—C11—C12	119.5 (2)
C9—Fe1—C6	68.03 (12)	C16—C11—N1	120.4 (2)
C7—Fe1—C6	40.23 (11)	C12—C11—N1	119.9 (2)
C3—Fe1—C8	107.69 (13)	C14—O1—C17	116.8 (3)
C2—Fe1—C8	118.47 (11)	C9—C10—Fe1	69.86 (17)
C10—Fe1—C8	67.85 (12)	C6—C10—Fe1	69.82 (16)
C4—Fe1—C8	127.47 (12)	C12—C13—C14	119.6 (2)
C9—Fe1—C8	40.20 (12)	C19—C20—C21	120.9 (3)
C7—Fe1—C8	40.41 (11)	C13—C12—C11	120.5 (3)
C6—Fe1—C8	67.84 (12)	C21—C22—C23	120.4 (2)
C3—Fe1—C5	68.16 (12)	C9—C8—C7	108.0 (3)
C2—Fe1—C5	68.13 (11)	C9—C8—Fe1	69.68 (17)
C10—Fe1—C5	109.30 (12)	C7—C8—Fe1	69.63 (16)
C4—Fe1—C5	40.57 (11)	C11—C16—C15	120.6 (3)
C9—Fe1—C5	128.55 (12)	C14—C15—C16	119.3 (3)
C7—Fe1—C5	153.13 (12)	C3—C4—C5	108.3 (2)
C6—Fe1—C5	119.96 (12)	C3—C4—Fe1	69.41 (16)
C8—Fe1—C5	165.55 (12)	C5—C4—Fe1	70.59 (15)
C3—Fe1—C1	68.23 (11)	C22—C23—C18	121.3 (2)
C2—Fe1—C1	40.51 (10)	O1—C14—C13	115.3 (3)
C10—Fe1—C1	127.92 (12)	C8—Fe1—C1	152.56 (11)
C4—Fe1—C1	68.06 (11)	C5—Fe1—C1	40.34 (10)
C9—Fe1—C1	165.82 (12)	C1—N1—C18	124.0 (2)

C7—Fe1—C1	118.78 (11)	C1—N1—C11	114.3 (2)
C6—Fe1—C1	108.18 (11)		

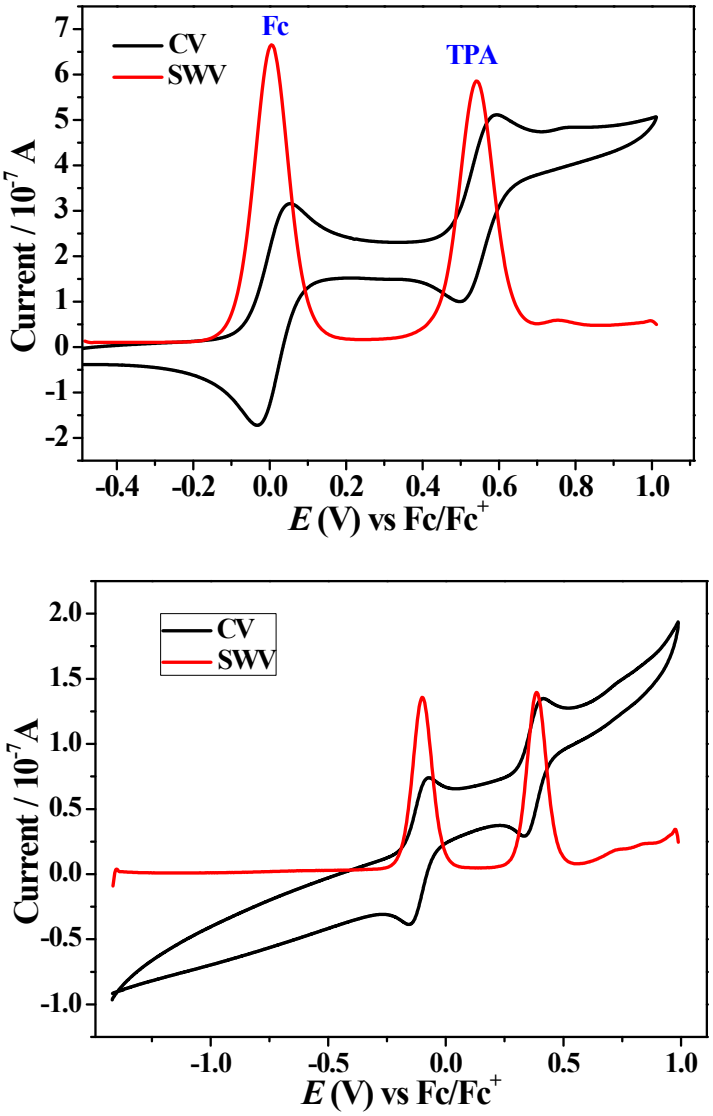

Figure S1. Cyclic voltammograms (CV, at v = 50 mV s^{-1}; black line) and corresponding square-wave voltammograms (SWV, at f = 10 Hz and t_p = 25 mV; red line) of TPA (top, with ferrocene present as the internal standard), and M4TPPD (bottom) in CH_2Cl_2/n-Bu_4NPF_6.

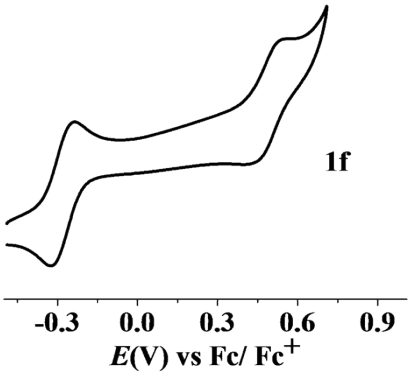

Figure S2. The curtailed two-anodic-step cyclic voltammogram (CV) of **1f** in CH_2Cl_2/*n*-Bu_4NPF_6 at v = 50 mV s^{-1}.

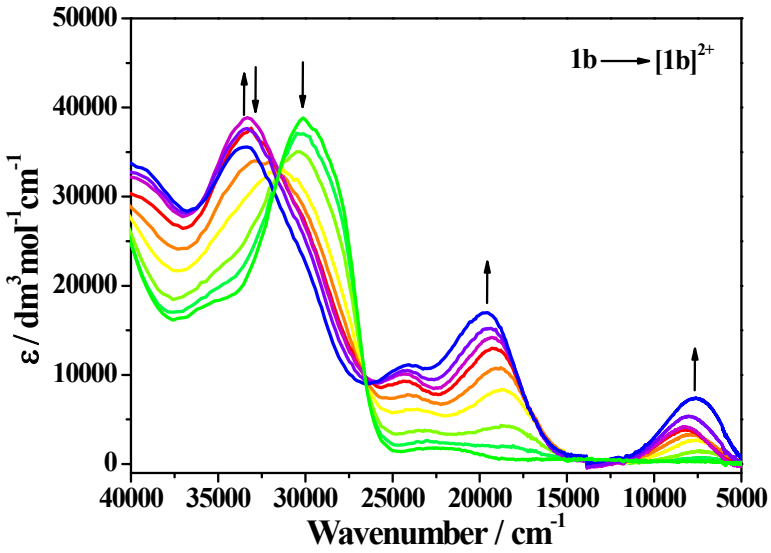

Figure S3. Changes in UV-vis-NIR absorption spectra recorded during the oxidation of complex **1b** to $[\mathbf{1b}]^{2+}$ in $CH_2Cl_2/10^{-1}$ M *n*-Bu_4NPF_6 at 298 K within an OTTLE cell. The intermediate absorption of $[\mathbf{1b}]^{+}$ is poorly resolved due to pronounced redox disproportionation of the monocation.

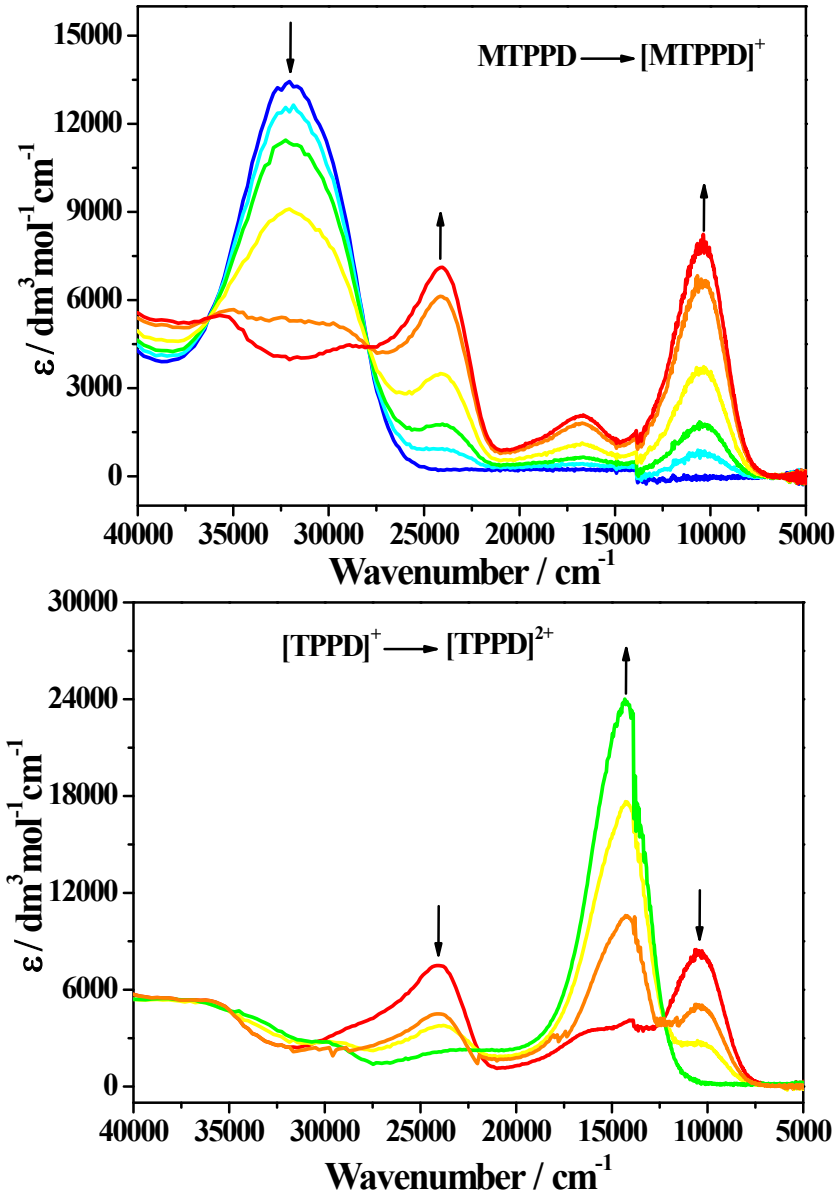

Figure S4. Changes in UV-vis-NIR absorption spectra recorded during the oxidation of reference compound **MTPPD** to [**MTPPD**]$^{+}$ (top) and [**MTPPD**]$^{2+}$ (bottom) in $CH_2Cl_2/10^{-1}$ M *n*-Bu_4NPF_6 at 298 K within an OTTLE cell.

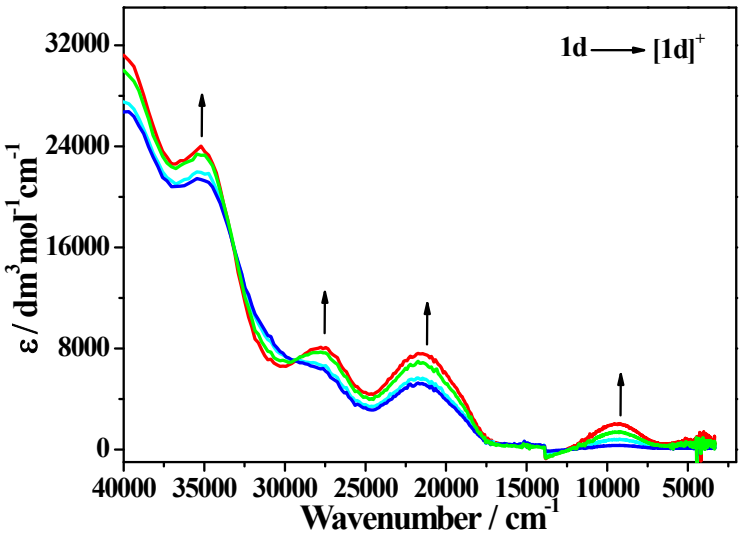

Figure S5. UV-vis-NIR spectral changes recorded during the reversible Fc-localized oxidation of complex **1d** to [**1d**]$^{+}$ in $CH_2Cl_2/10^{-1}$ M *n*-Bu_4NPF_6 at 298 K within an OTTLE cell.

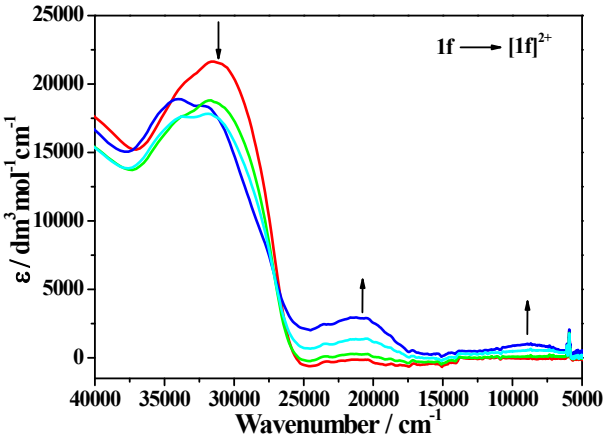

Figure S6. Changes in UV-vis-NIR absorption recorded during the unresolved bielectronic oxidation of dinuclear complex **1f** to [**1f**]$^{2+}$ in $CH_2Cl_2/10^{-1}$ M *n*-Bu_4NPF_6 at 298 K within an OTTLE cell. The subsequent oxidation to [**1f**]$^{3+}$ was complicated by low solubility of the ultimate product.

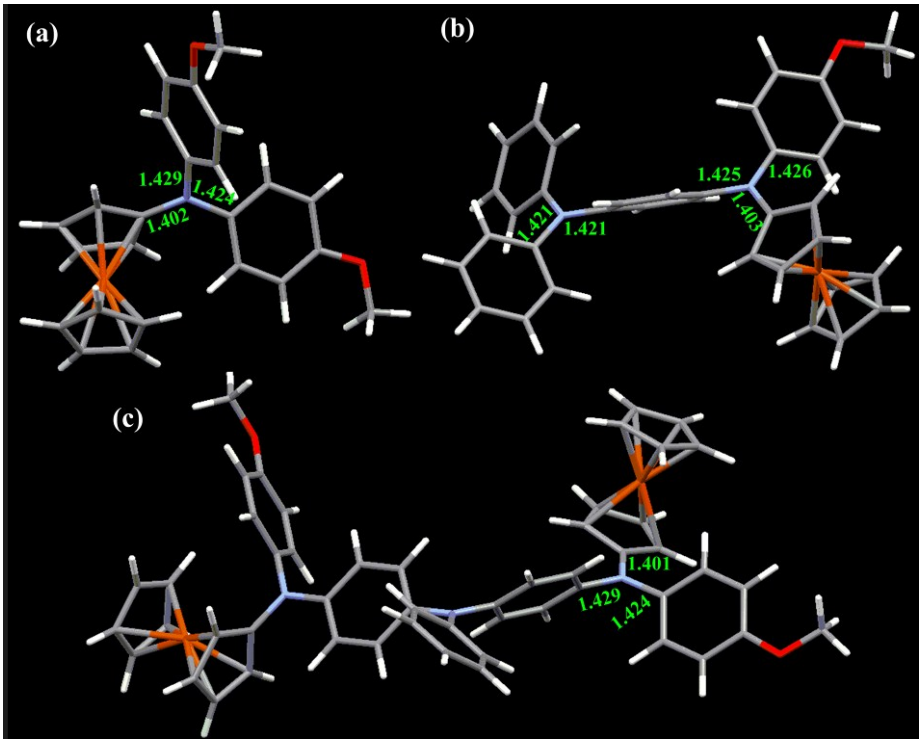

Figure S7. The DFT-optimized geometric structures of **1d** (a), **1e** (b) and **1f** (c).

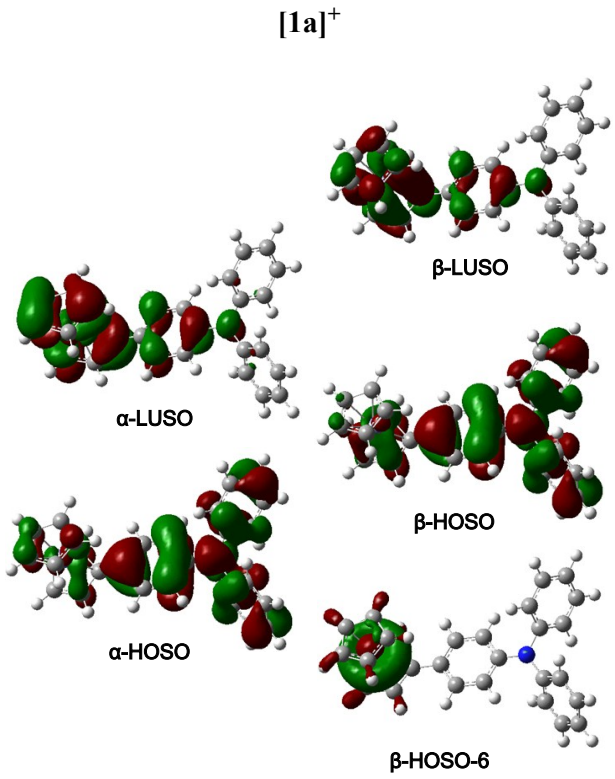

Figure S8. Spin orbitals involved in the major electronic excitations of [**1a**]$^{+}$. B3LYP /6-31G* (Fe: Lanl2DZ) /CPCM /CH_2Cl_2.

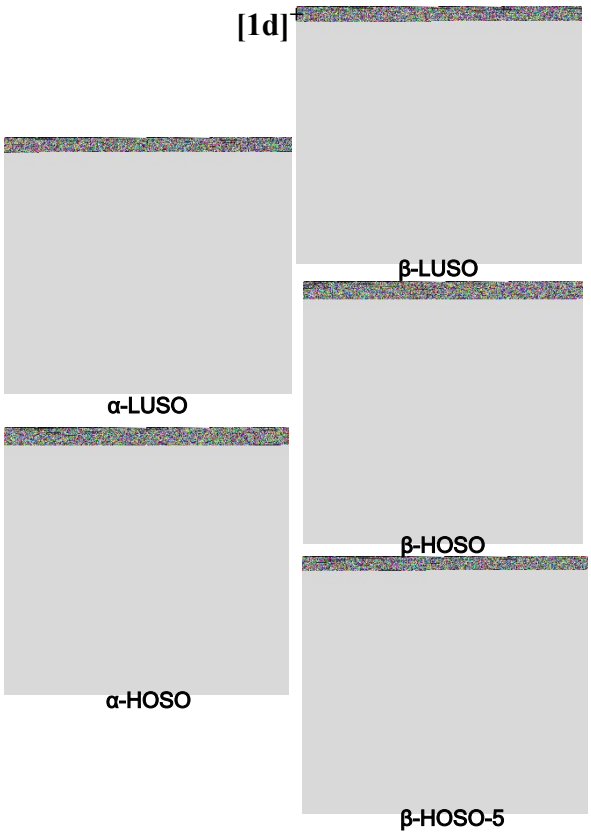

Figure S9. Spin orbitals involved in the major electronic excitations of [**1d**]$^{+}$. B3LYP /6-31G* (Fe: Lanl2DZ) /CPCM /CH_2Cl_2.

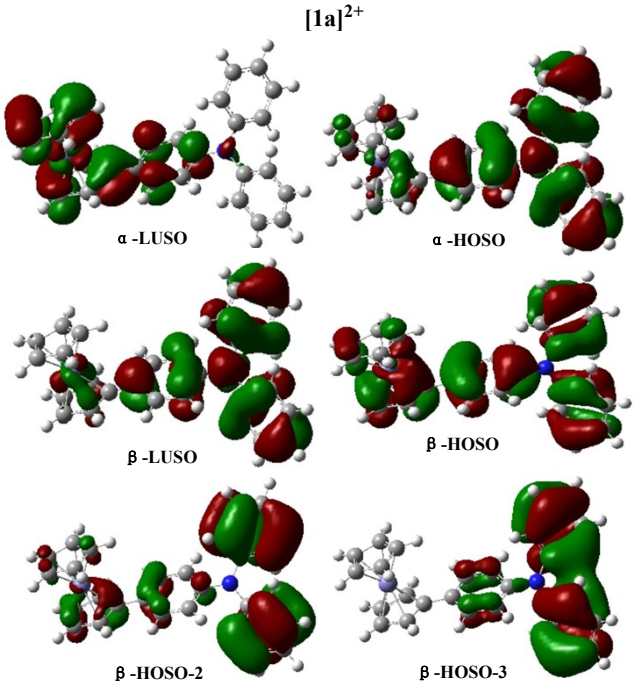

Figure S10. Spin orbitals involved in the major electronic excitations of [**1a**]$^{2+}$ (biradical state). B3LYP /6-31G* (Fe: Lanl2DZ) /CPCM /CH_2Cl_2.

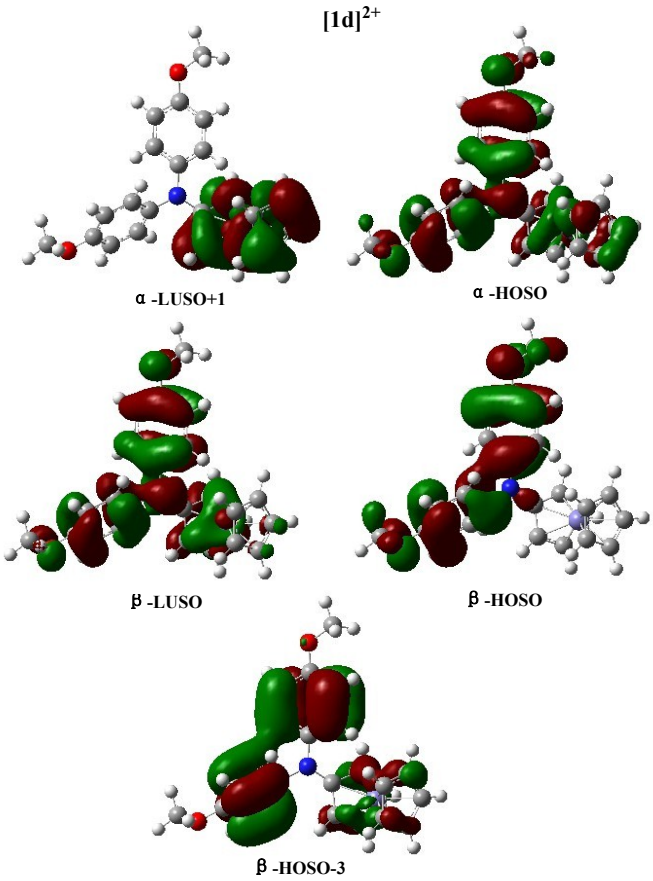

Figure S11. Spin orbitals involved in the major electronic excitations of [**1d**]$^{2+}$ (biradical state).

B3LYP /6-31G* (Fe: Lanl2DZ) /CPCM /CH_2Cl_2.

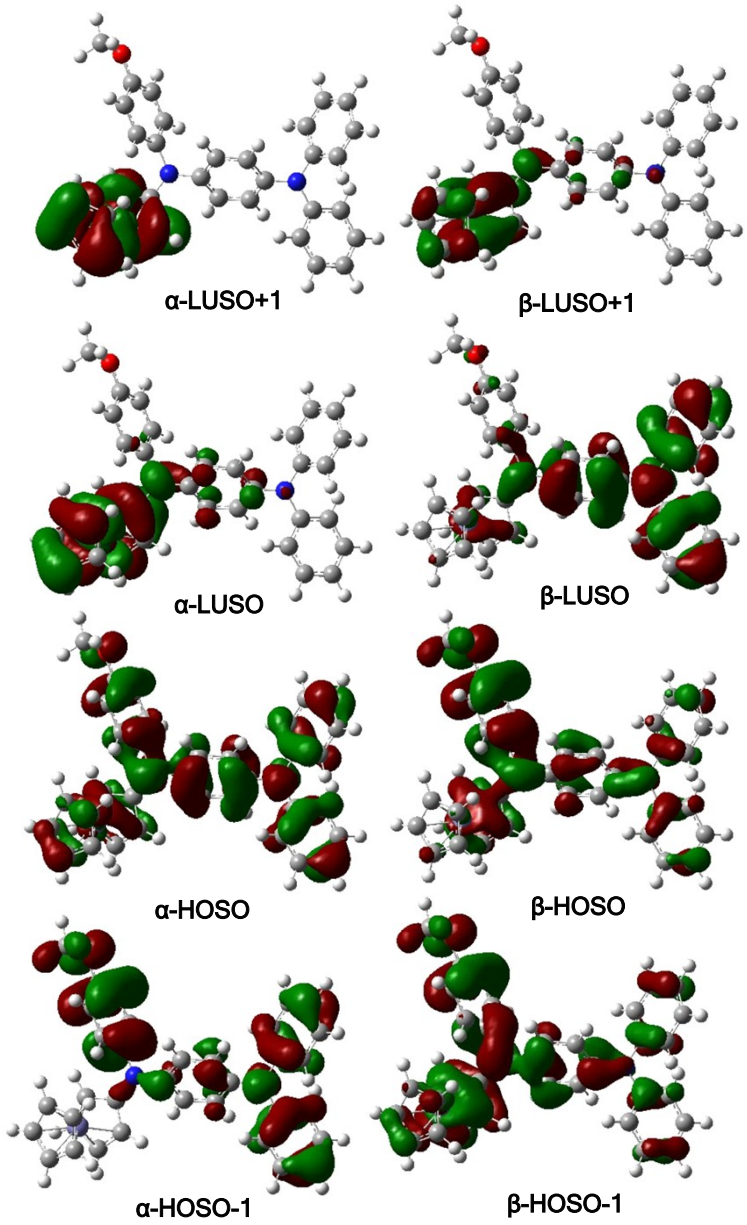

Figure S12. Frontier spin orbitals of [**1e**]$^{2+}$ (biradical state). B3LYP /6-31G* (Fe: Lanl2DZ) /CPCM /CH_2Cl_2.

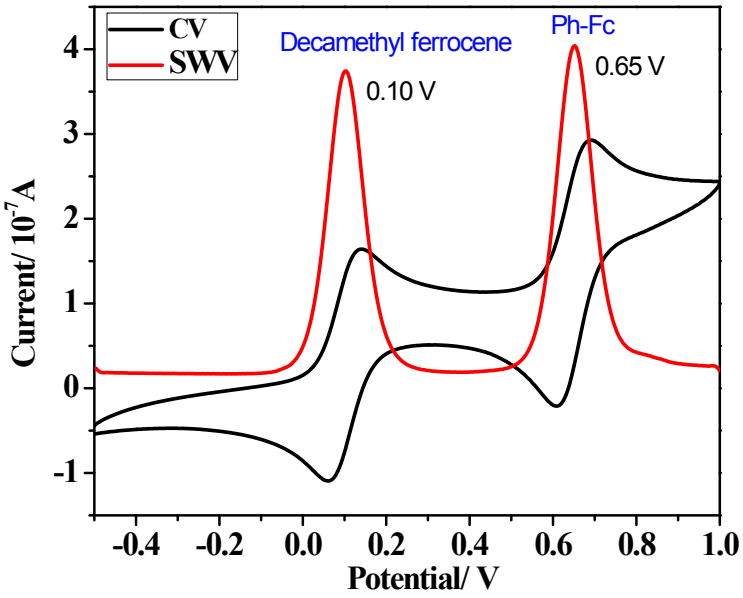

Figure S13. The cyclic voltammogram (CV, black line; v = 50 mV s^{-1}) and the corresponding square-wave voltammogram (SWV, red line; at f = 10 Hz and t_p = 25 mV) of reference phenylferrocene, Ph-Fc, in CH_2Cl_2/*n*-Bu_4NPF_6. The oxidation potential of Ph-Fc is $E_{1/2}$ = +0.04 V vs ferrocene/ferrocenium (Fc/Fc^+). The electronic absorption of $[Ph\text{-}Fc]^+$ is presented in Figure S14.

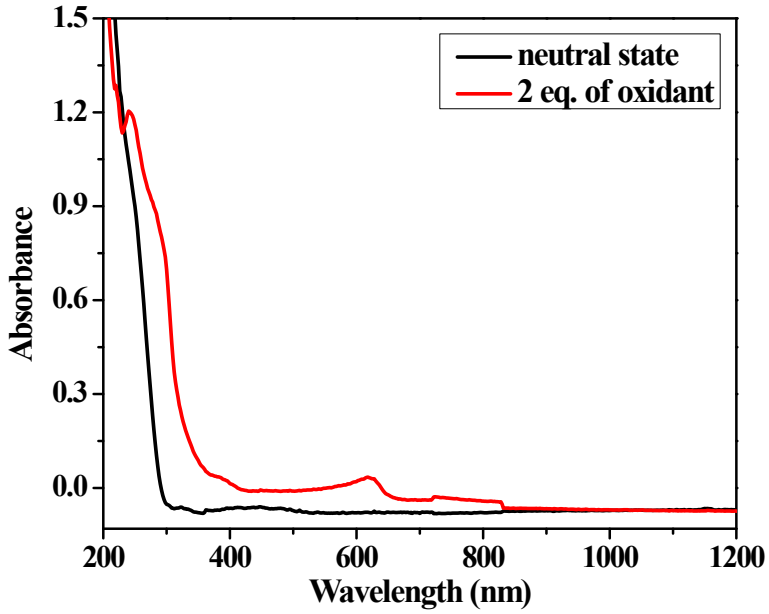

Figure S14. Electronic absorption spectra of 10^{-2} M Ph-Fc (black line) and $[Ph\text{-}Fc]^+$ (red line) obtained by chemical oxidation with $AgPF_6$ in CH_2Cl_2 at 298 K. The simulated spectra of $[Ph\text{-}Fc]^+$ and corresponding electronic transitions obtained with TD-DFT methods are depicted in Figures S15-S17.

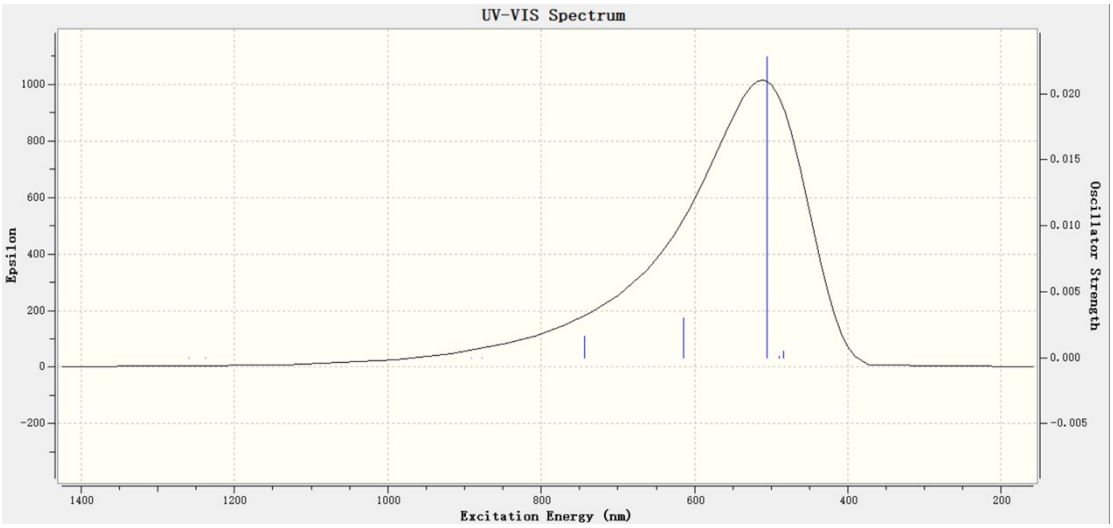

Figure S15. Simulated electronic absorption of $[Ph\text{-}Fc]^+$. B3LYP/6-31G*/CPCM /CH_2Cl_2.

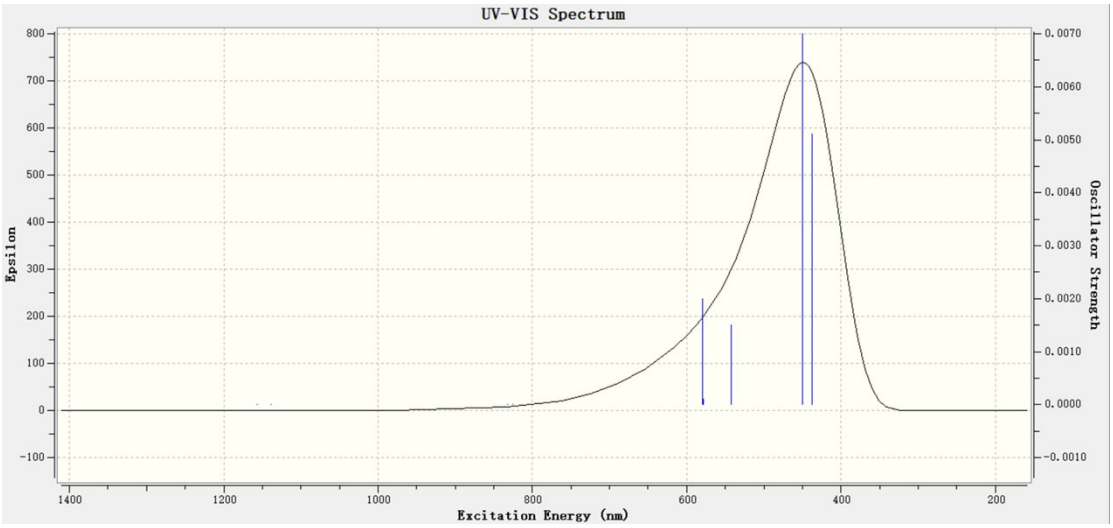

Figure S16. Simulated electronic absorption of $[Ph\text{-}Fc]^+$; CAM-B3LYP/6-31G*/CPCM /CH_2Cl_2.

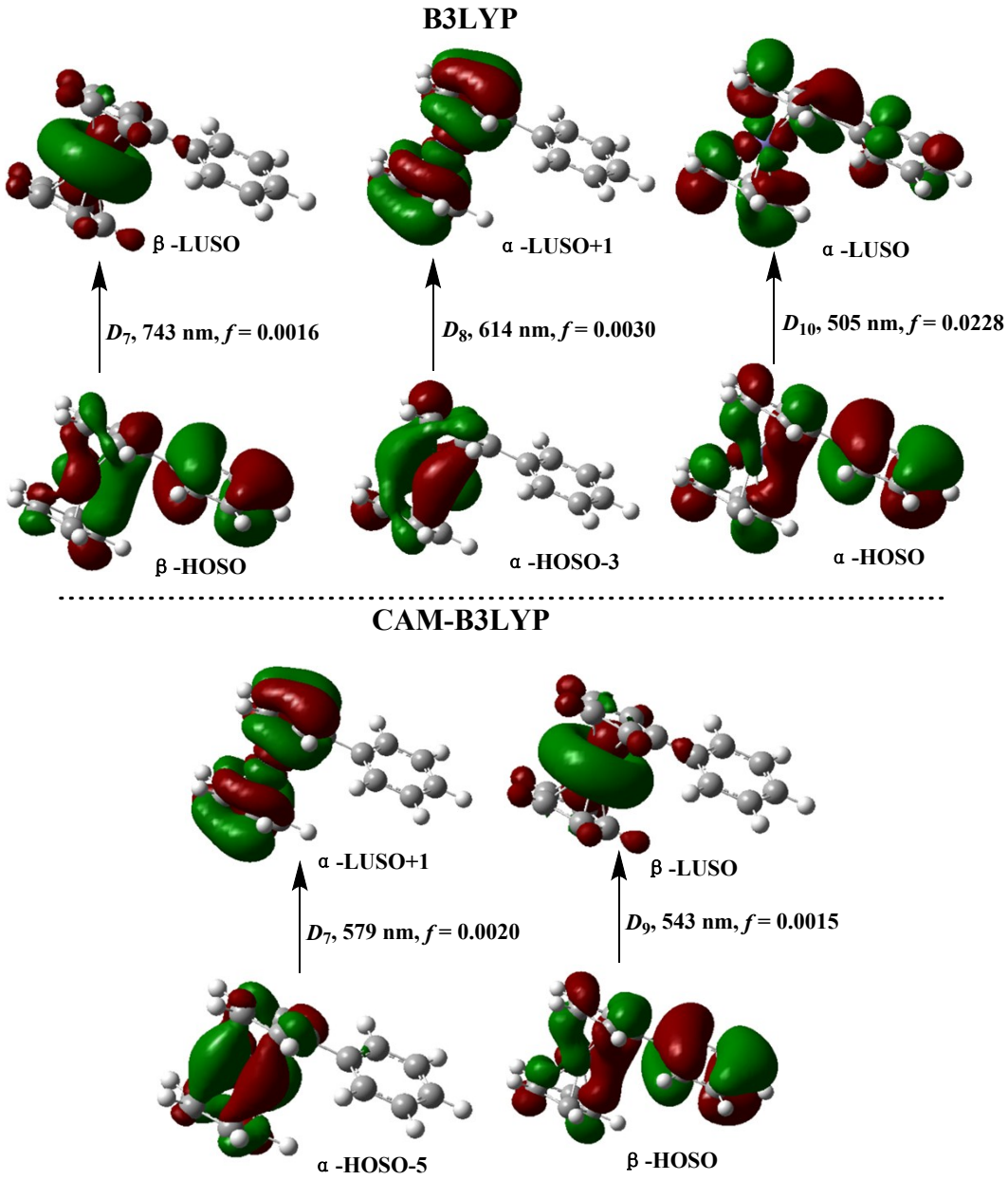

Figure S17. Spin orbitals involved in the plausible calculated visible electronic excitations of [Ph-Fc]$^+$ (see Figures S15 and S16). A better agreement with the experimental visible absorption of the cationic complex has been reached with the B3LYP method.

NMR Spectra

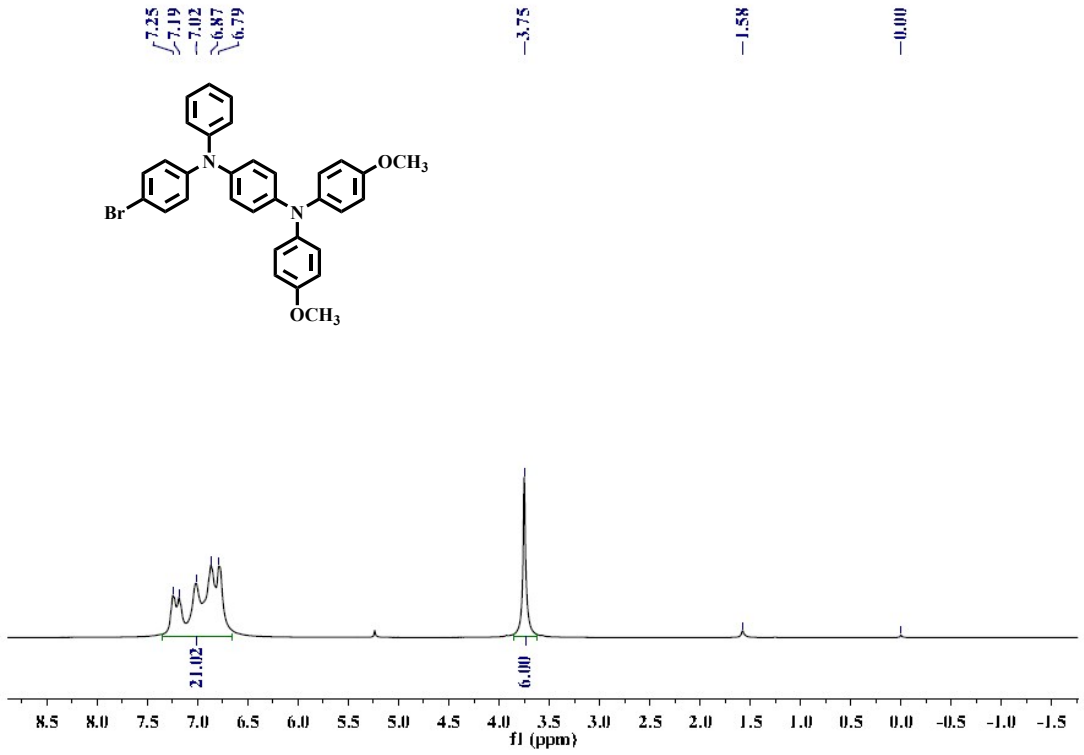

Figure S18. ^{1}H NMR spectrum (400 MHz, $CDCl_3$) of **2c**.

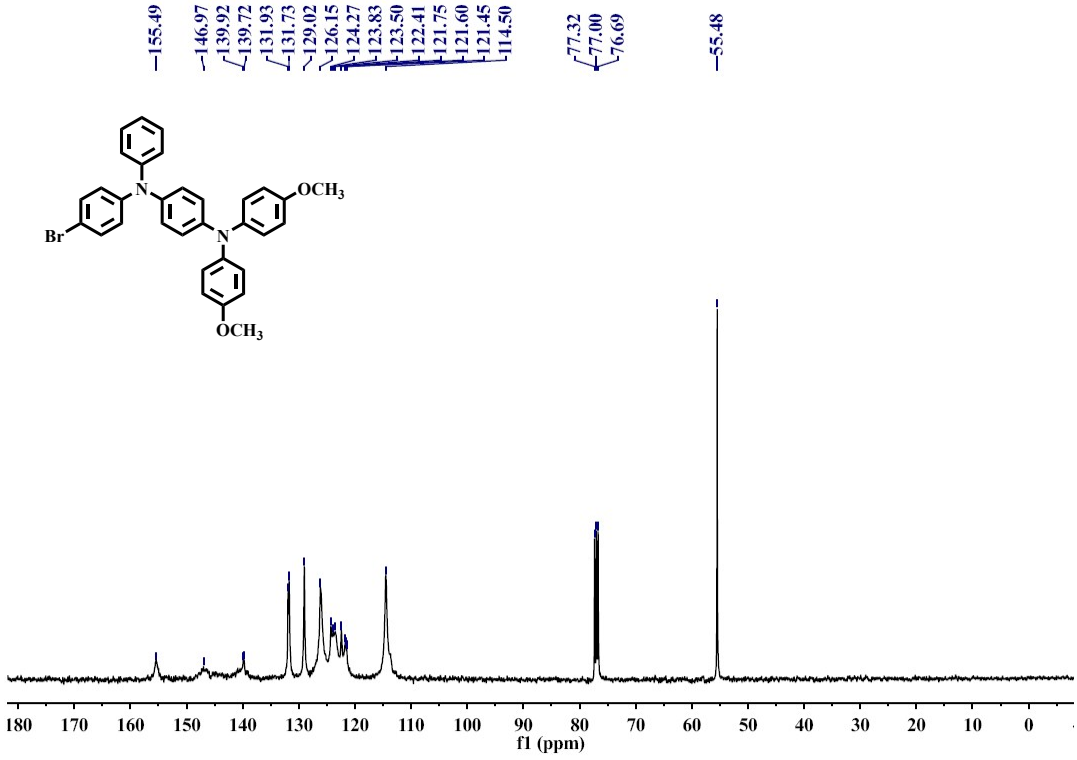

Figure S19. ^{13}C NMR spectrum (100 MHz, $CDCl_3$) of **2c**.

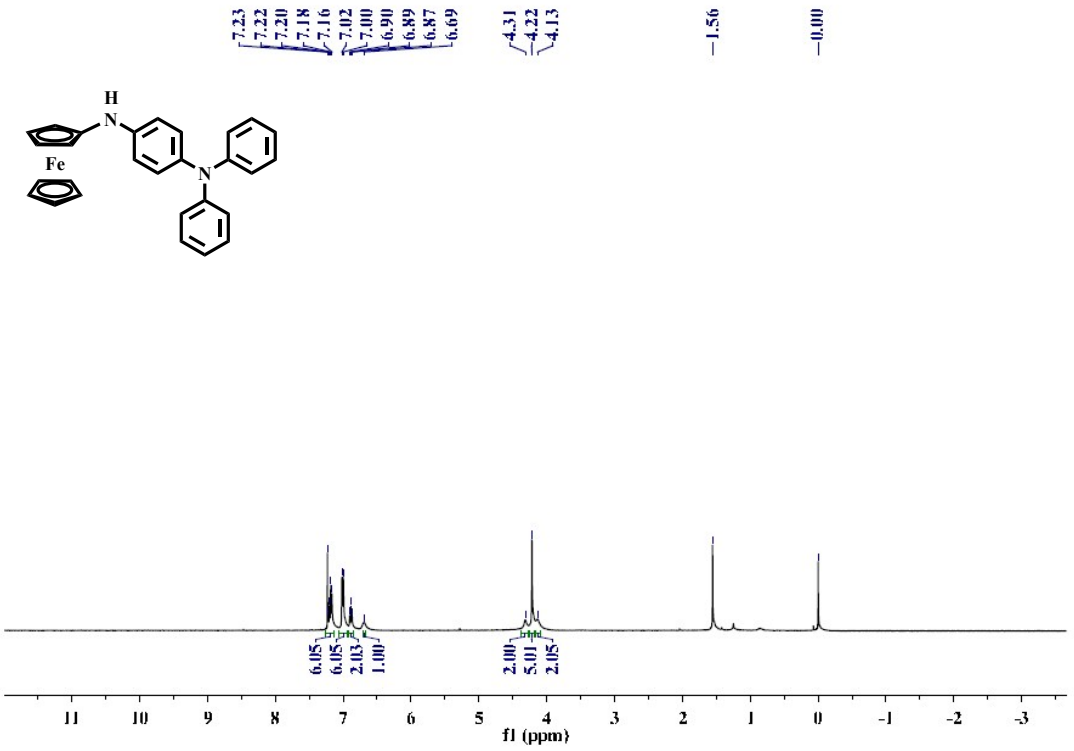

Figure S20. ^{1}H NMR spectrum (400 MHz, $CDCl_3$) of **2e**.

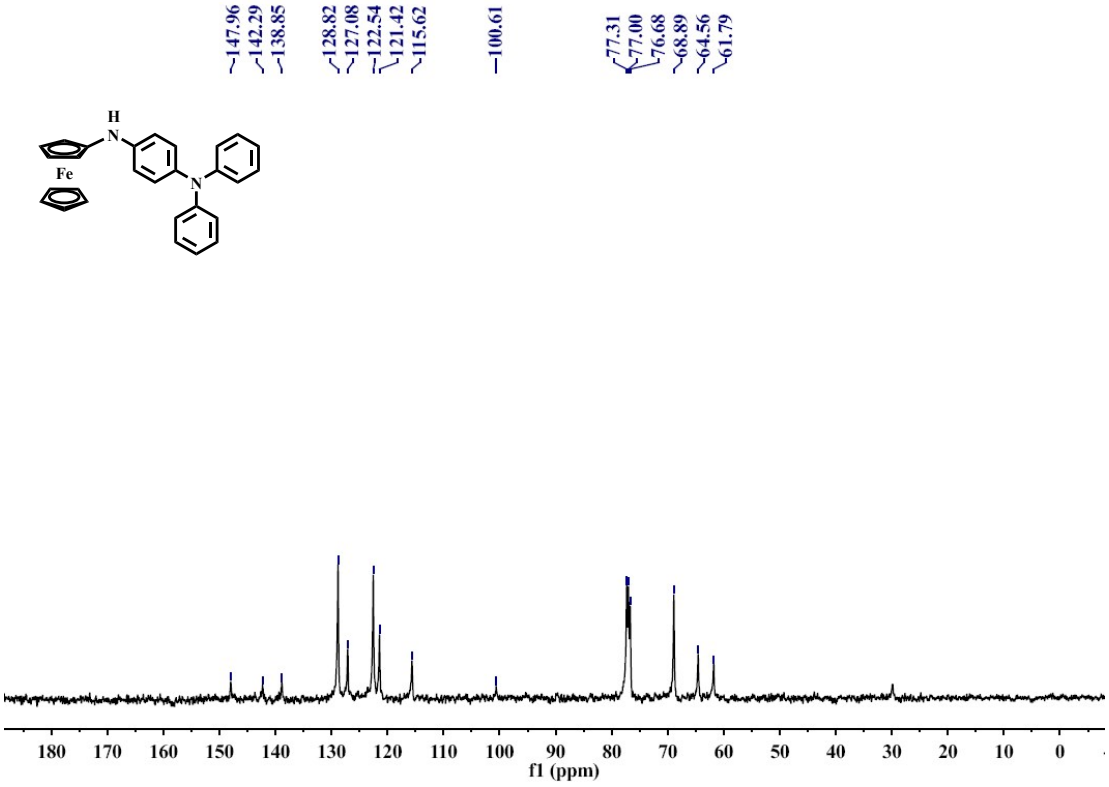

Figure S21. ^{13}C NMR spectrum (100 MHz, $CDCl_3$) of **2e**.

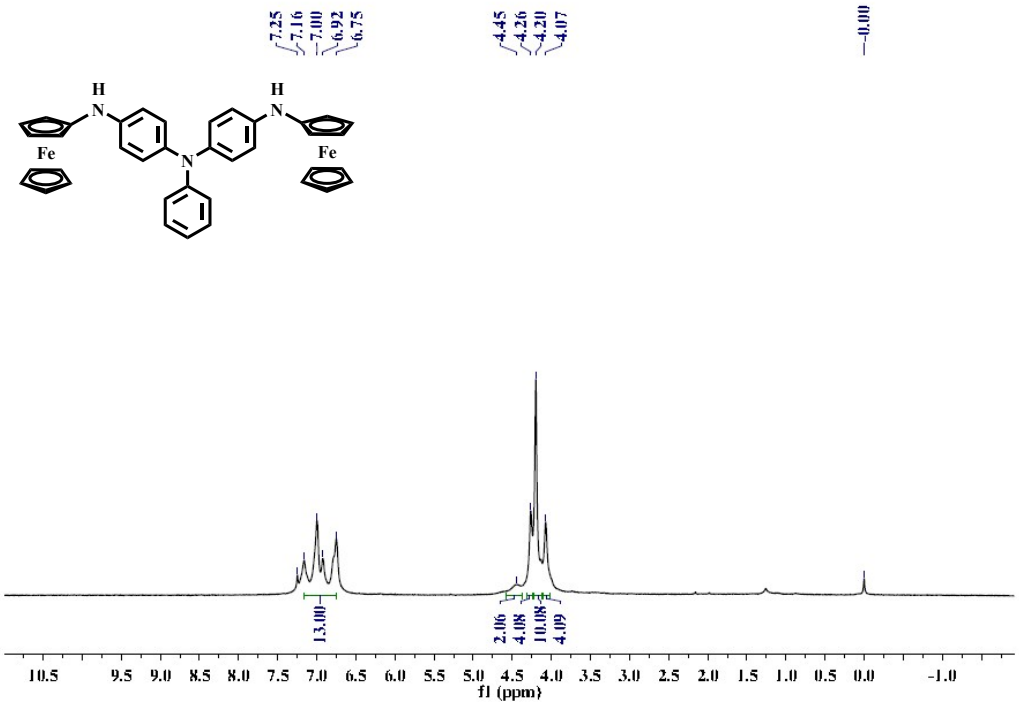

Figure S22. ^{1}H NMR spectrum (600 MHz, $CDCl_3$) of **2f**.

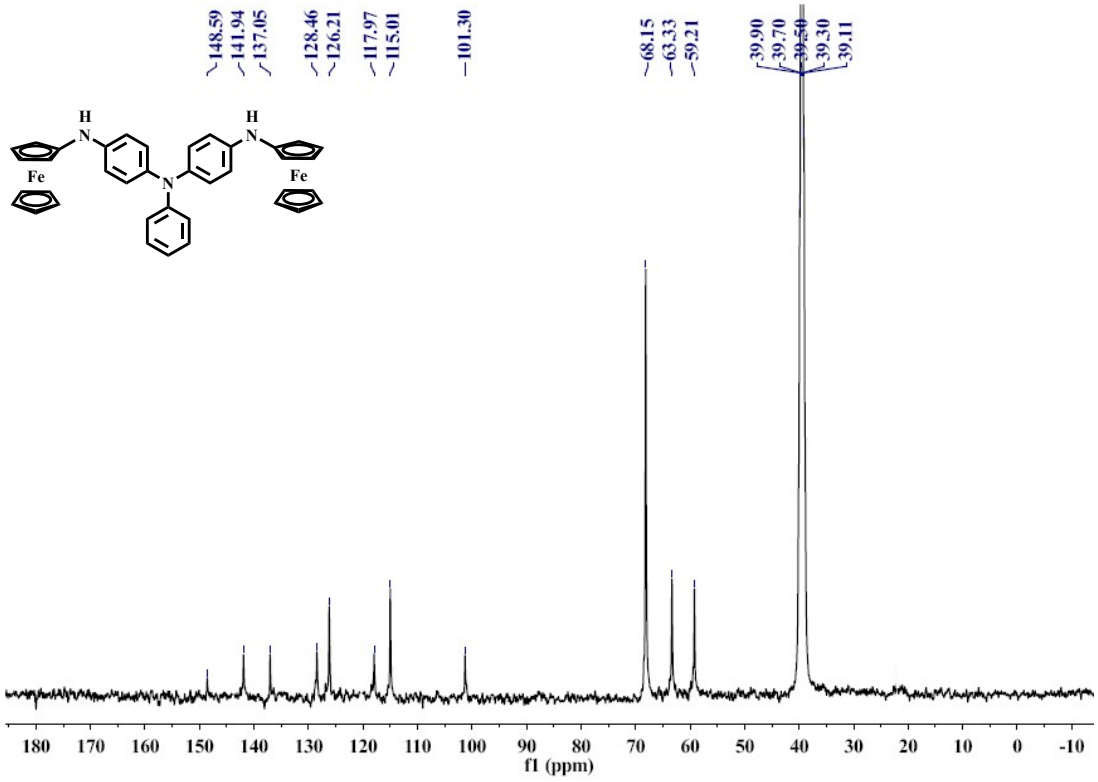

Figure S23. ^{13}C NMR spectrum (100 MHz, DMSO-d_6) of **2f**.

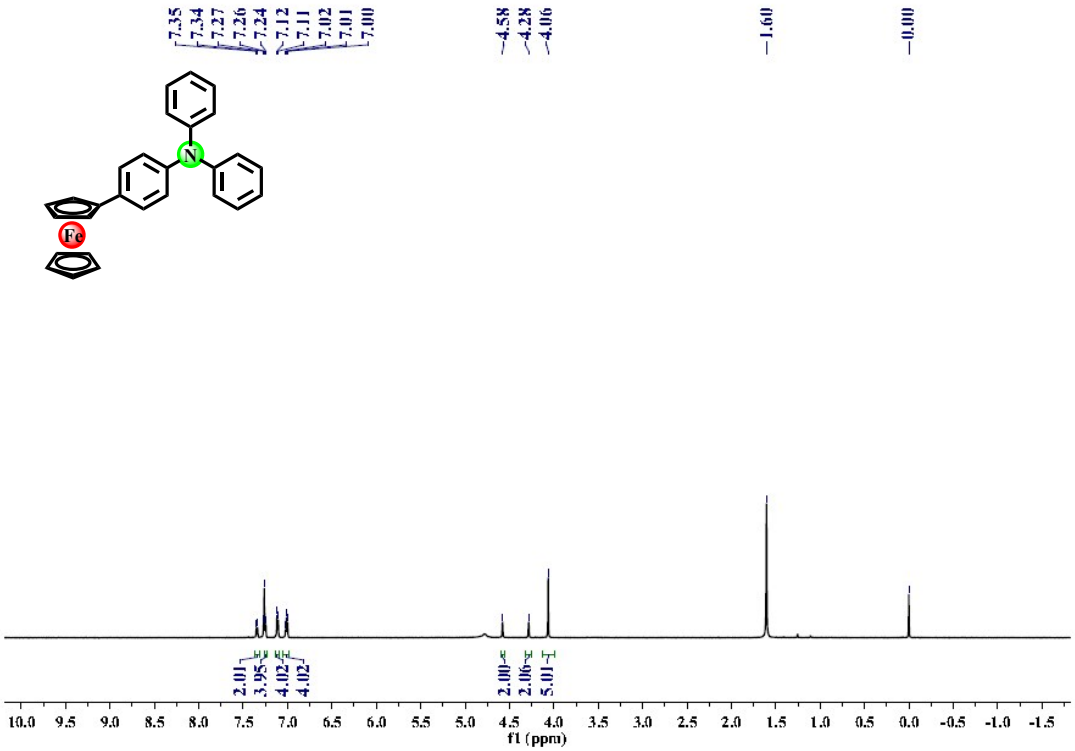

Figure S24. ^{1}H NMR spectrum (400 MHz, $CDCl_3$) of **1a**.

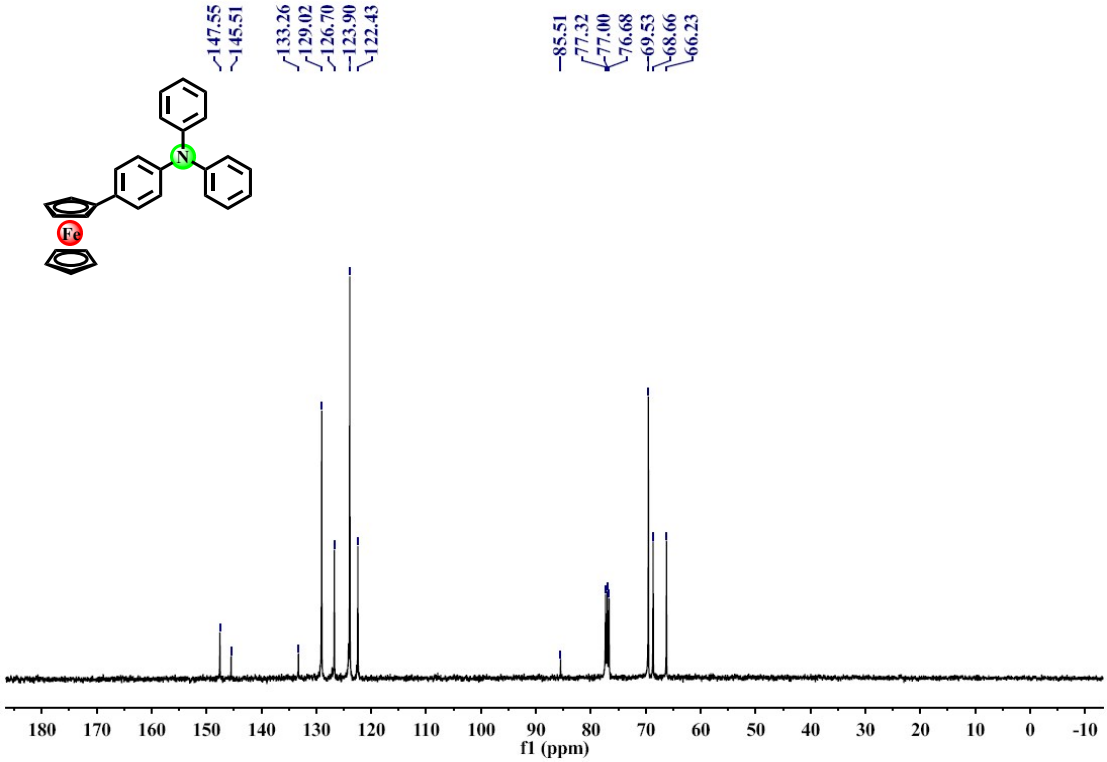

Figure S25. ^{13}C NMR spectrum (100 MHz, $CDCl_3$) of **1a**.

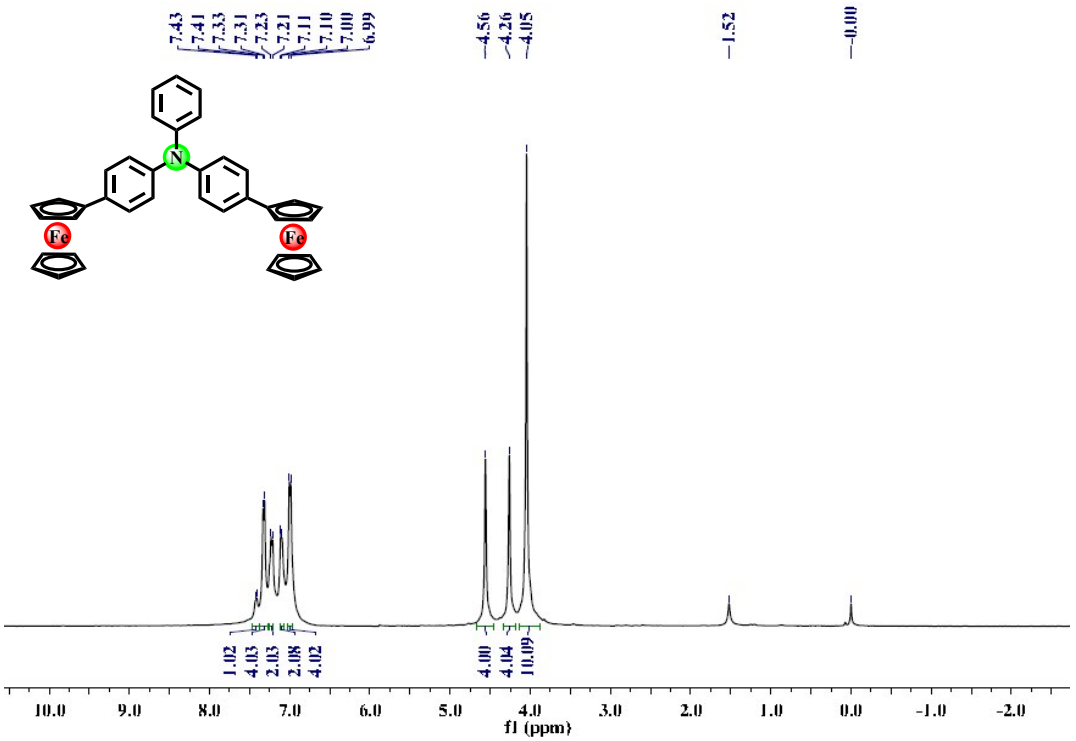

Figure S26. ^{1}H NMR spectrum (400 MHz, $CDCl_3$) of **1b**.

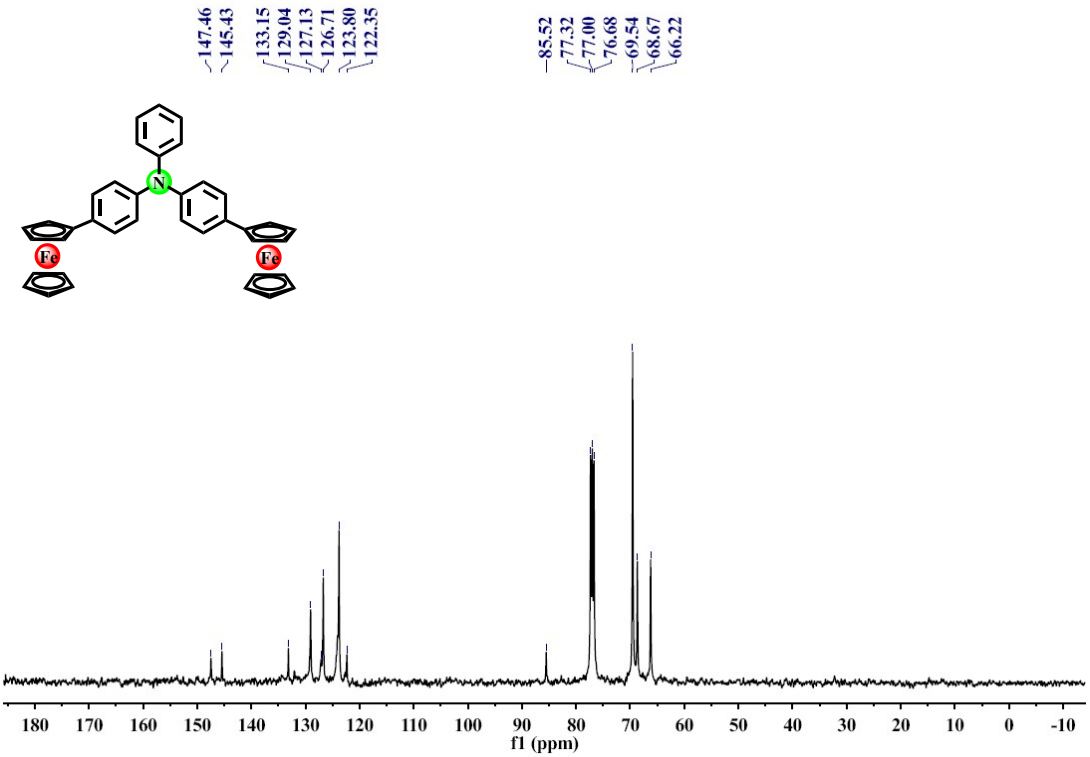

Figure S27. ^{13}C NMR spectrum (100 MHz, $CDCl_3$) of **1b**.

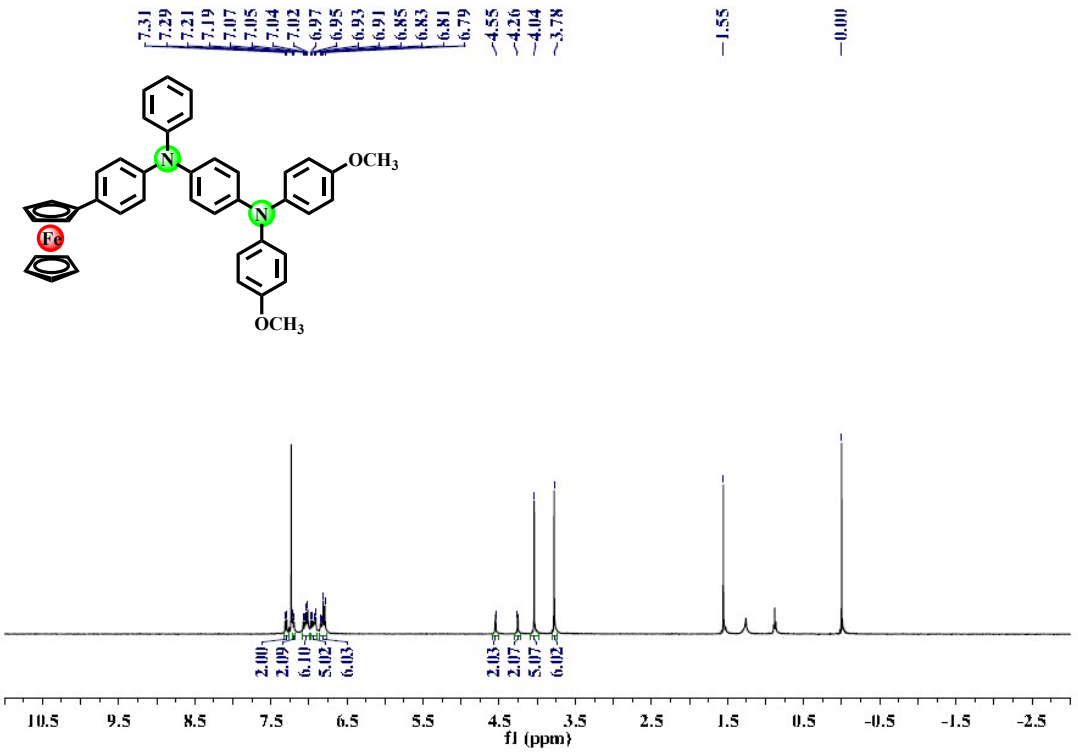

Figure S28. ^{1}H NMR spectrum (400 MHz, $CDCl_3$) of **1c**.

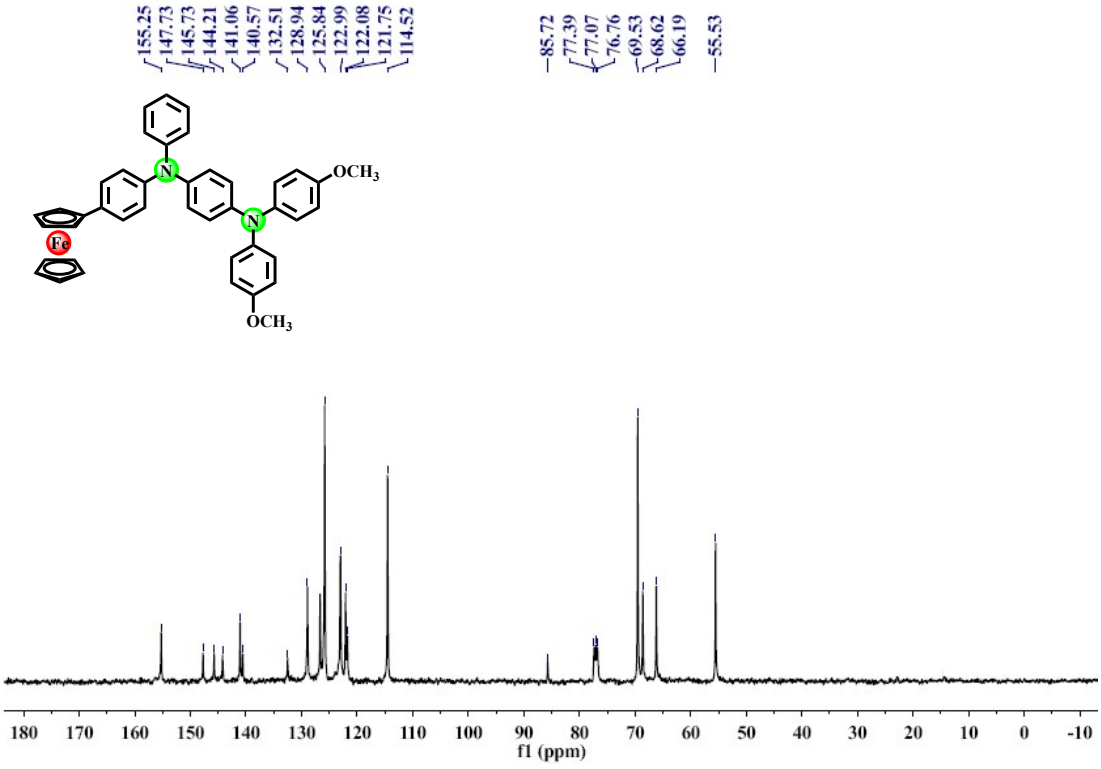

Figure S29. ^{13}C NMR spectrum (100 MHz, $CDCl_3$) of **1c**.

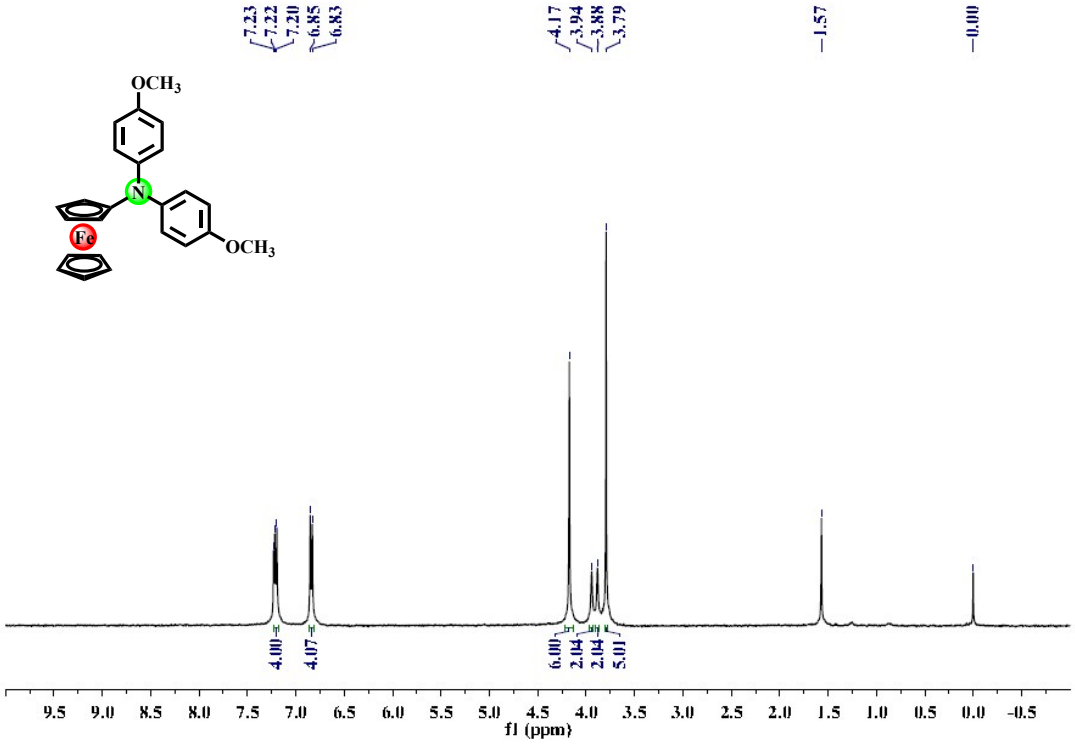

Figure S30. ^{1}H NMR spectrum (400 MHz, $CDCl_3$) of **1d**.

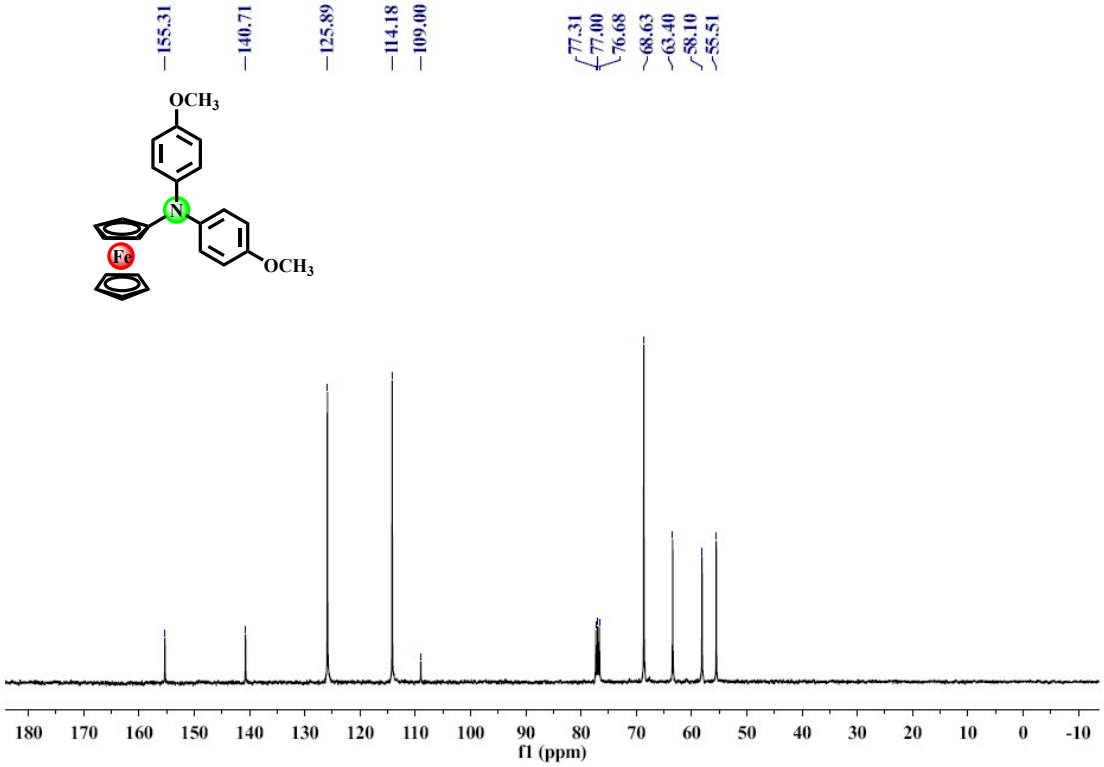

Figure S31. ^{13}C NMR spectrum (100 MHz, $CDCl_3$) of **1d**.

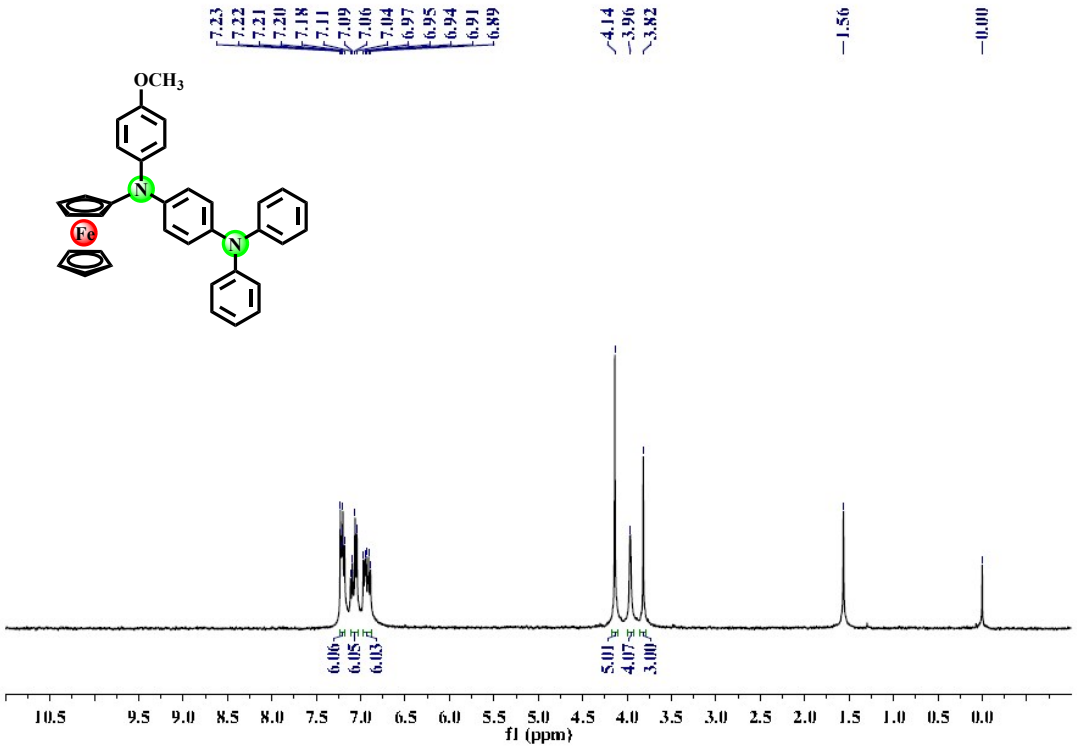

Figure S32. ^{1}H NMR spectrum (400 MHz, $CDCl_3$) of **1e**.

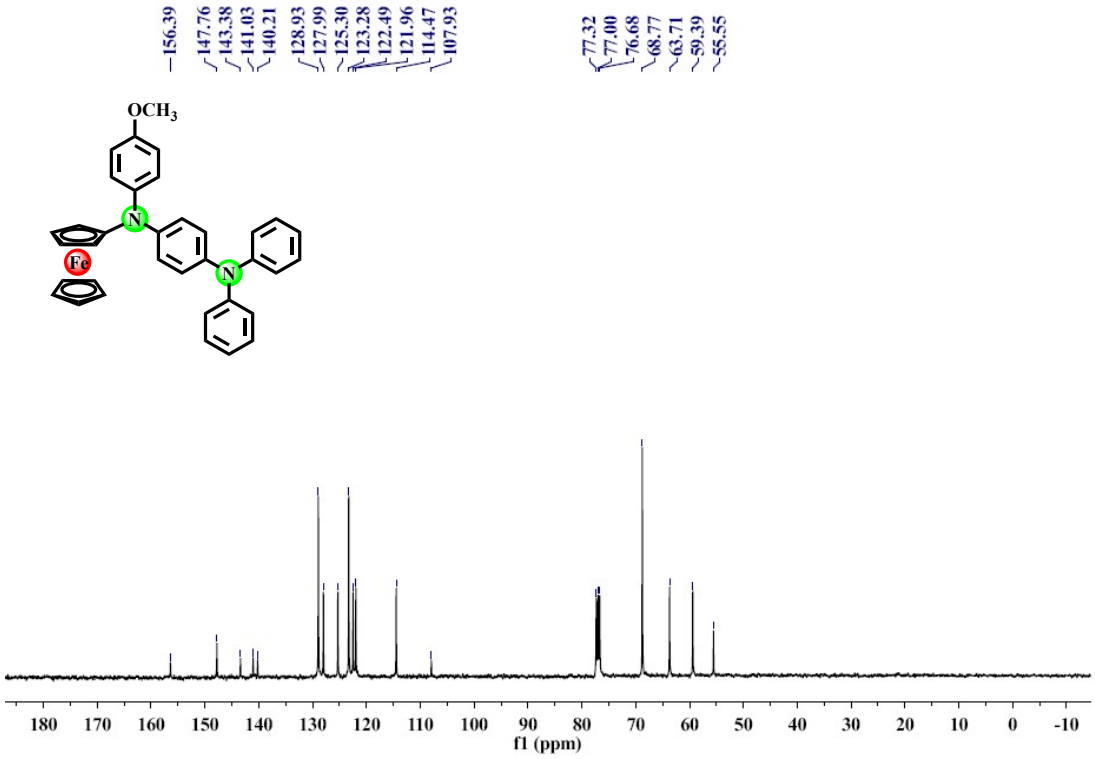

Figure S33. ^{13}C NMR spectrum (100 MHz, $CDCl_3$) of **1e**.

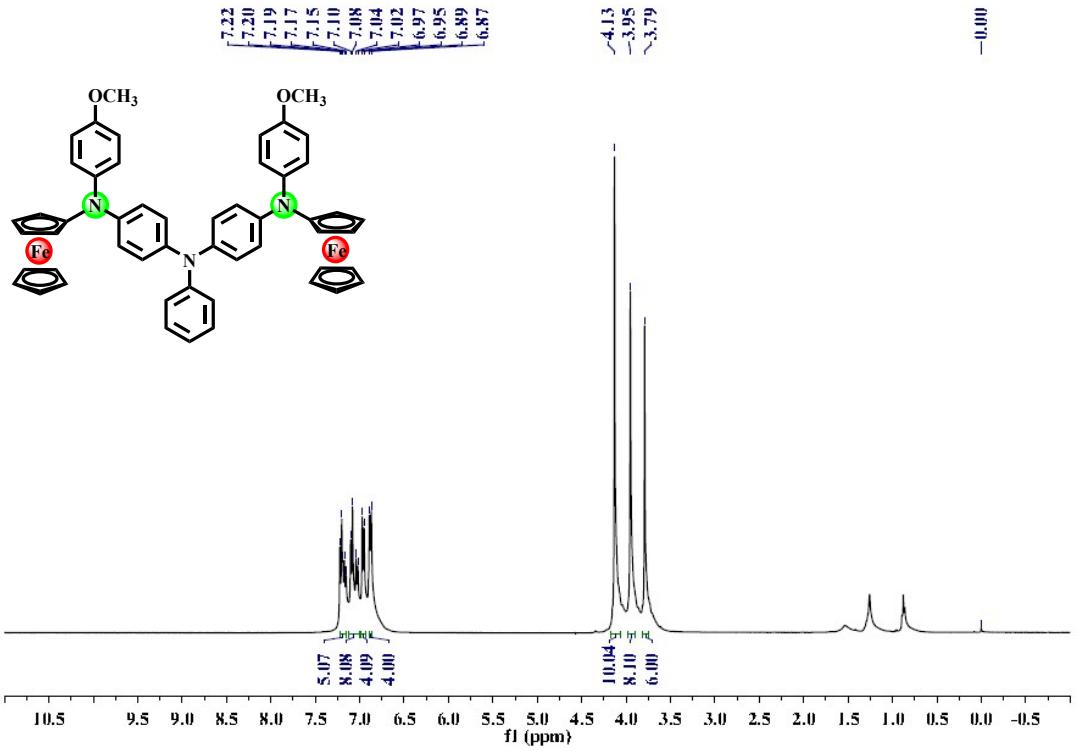

Figure S34. ^{1}H NMR spectrum (400 MHz, $CDCl_3$) of **1f**.

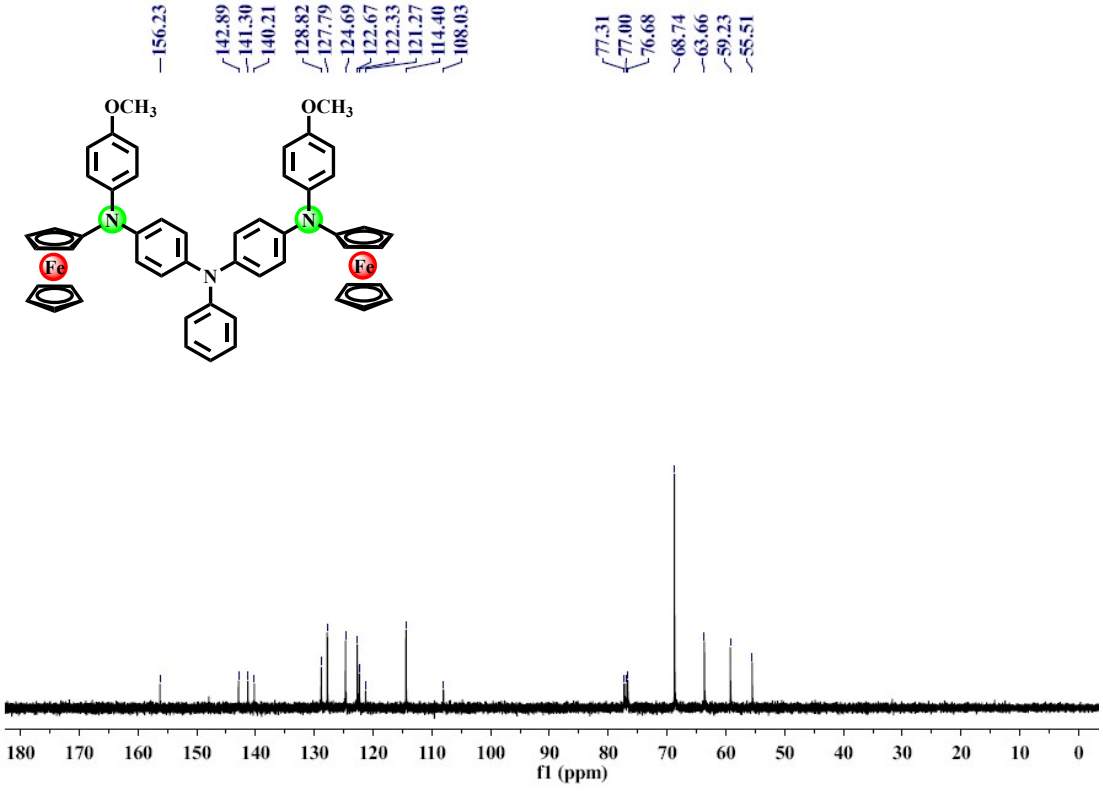

Figure S35. ^{13}C NMR spectrum (100 MHz, $CDCl_3$) of **1f**.